



Equidistant ($f\theta$) fish-eye perspective with application in distortion centre estimation

Ciarán Hughes^{a,*}, Robert McFeely^a, Patrick Denny^b, Martin Glavin^a, Edward Jones^a

^a Connaught Automotive Research Group, Department of Electronic Engineering, National University of Ireland, University Road, Galway, Ireland

^b Valeo Vision Systems, I.D.A. Business Park, Dunmore Road, Tuam, County Galway, Ireland

ARTICLE INFO

Article history:

Received 8 December 2008

Received in revised form 14 August 2009

Accepted 14 September 2009

Keywords:

Fish-eye

Perspective

Equidistant projection

Camera calibration

Distortion centre

ABSTRACT

Radial distortion in an image is a geometric distortion that causes a non-linear variation in resolution across the image, with a higher spatial resolution in the central areas of the image, and lower resolution in the peripheral areas of the image. This is particularly evident in fish-eye cameras, with very wide fields-of-view. Equidistant fish-eye cameras are designed such that the distance between a projected point and the distortion centre of the image is proportional to the incident angle of the projected ray, scaled only by the focal length. The perspective of the projection of a given scene in an equidistant fish-eye camera differs greatly from the projection of the same scene in a rectilinear pin-hole camera. For example, while the field-of-view is significantly larger for a fish-eye camera, the non-linear radial distortion of the scene results in straight lines mapping to curves of a particular shape in the equidistant fish-eye image.

In this paper, we describe equidistant fish-eye perspective in terms of the projection of sets of parallel lines to the equidistant fish-eye plane, and derive an equation that describes the projection of a straight line. We also demonstrate how the shape of a projected straight line can be accurately described by arcs of circles on the distorted image plane. We also describe an application of the equidistant perspective properties, by showing that the distortion centre of an equidistant fish-eye camera can be estimated by the extraction of the vanishing points. Additionally, we examine the accuracy of this estimation procedure on a large set of synthetically created images and a smaller set of real images from fish-eye cameras.

© 2009 Elsevier B.V. All rights reserved.

1. Introduction

Radial lens distortion causes points on the image plane to be displaced in a nonlinear fashion from their ideal position in the rectilinear pin-hole camera model, along a radial axis from the distortion centre in the equidistant image plane. The visual effect of this displacement in fish-eye optics is that the image will have a higher resolution in the foveal areas, with the resolution decreasing non-linearly towards the peripheral areas of the image. Equidistant fish-eye cameras are designed such that the distance between a projected point and the distortion centre of the image is proportional to the incident angle of the projected ray, scaled only by the focal length. A commonly used model of radial distortion is the odd-ordered polynomial model [1–5]. However, due to the particularly high levels of distortion present in fish-eye cameras, there have been several alternative models developed, including the *Fish-Eye Transform* [6], the *Polynomial Fish-Eye Transform* [6], the *Field Of View model* [7], the *Division model* [8,9] and the *Rational Function model* [10–12].

In the projection of a set of parallel lines to the image plane using the rectilinear pin-hole perspective model, the straight lines are imaged as straight lines and parallel sets of straight lines converge at a single *vanishing point* on the rectilinear image plane. However, we will show that, in equidistant fish-eye perspective, the projection of a parallel set of lines in real-world coordinates will be a set of curves that converge at two vanishing points, and that the line that intersects the two vanishing points will also intersect the distortion centre of the camera. Additionally, by analysing how accurately the Division model of radial distortion models the distortion present in equidistant fish-eye cameras, we demonstrate that the curves that describe projected lines can be accurately estimated as circles on the equidistant image plane, and from this we demonstrate how the distortion centre can be accurately estimated. The importance of the correct estimation of the distortion centre is well established [13], and assuming that the distortion centre is collocated with the image frame centre is inaccurate, and can lead to visible artifacts if the image is corrected, as we demonstrate in Section 3.3.

In Section 2, we describe some properties of the projection of parallel lines onto both the rectilinear image plane and the distorted equidistant image plane, and describe some of the characteristics of this perspective. However, it is shown that the projection

* Corresponding author. Tel.: +353 91 49 2605; fax: +353 91 49 4511.

E-mail addresses: ciaran.hughes@nuigalway.ie, ciaran.hughes@valeo.com (C. Hughes).

of a straight line under the equidistant mapping function has a complicated form. To get a practical approximation, in Section 2.3 we will show that a much simplified projection shape (a circle) can be used, as the projection of a line under the division model of radial distortion is a circle. The use of this fact necessitates the validation of the division model and an examination of its accuracy when used with fish-eye cameras that are manufactured to the equidistant mapping function, which is also completed in Section 2.3. In Section 3, we describe a distortion centre estimation procedure based on the extraction of vanishing points using circle fitting to sets of parallel lines, and examine the accuracy of the algorithm using sets of synthetic and real calibration images.

2. The perspective of camera projections

There has been some work done in the area of camera calibration using perspective principles, in particular vanishing point extraction. However, there has been little work specifically on equidistant fish-eye camera calibration using vanishing point extraction and other features of equidistant perspective. In applying camera perspective principles to camera calibration, both Cipolla et al. [14] and Daniilidis and Ernst [15] describe methods using rectilinear pin-hole perspective to extract the principal point, and other camera calibration parameters for rectilinear cameras. Cipolla et al. [14] manually extract the real-world parallel edges from the image to find three vanishing points, and thus find the distortion centre as the orthocentre of the triangle formed by those vanishing points. Daniilidis and Ernst [15] use the fact that under camera motion a vanishing point traverses a conic section on the image plane. The coefficients of the conic section can be used to deduce the intrinsic parameters of the camera. More recent work on the calibration of cameras using perspective principles has been done in, for example [16–18]. However, none of these publications address cameras in which radial distortion is an issue. That is, the calibrations described assume that the cameras follow the pin-hole projection mapping function.

Zheng and Li [19] describe a method by which the roll, tilt and yaw of the camera are determined by extracting the vanishing points of parallel lines in a fish-eye camera. However, they do not determine any of the intrinsic parameters of the camera, and fail to fully describe the perspective of the fish-eye camera. Ying et al. [20] describe a method of calibrating cameras with radial distortion using spherical perspective projection principles. However, because they use orthographic spherical perspective projection, their algorithms only apply to orthographic fish-eye cameras ($r = f \sin \theta$), and cannot accurately be applied to equidistant fish-eye cameras ($r = f\theta$).

Geyer and Daniilidis [21] use vanishing point extraction to determine the parameters of a wide-angle paracatadioptric camera system. Paracatadioptric camera systems involve the use of a combination of a parabolic reflective element and a lensed camera. It is also shown that the projection of a line under such a system results in a circular arc on the image plane, which is the same result as the projection of a line under the division model (see Section 2.3). The similarities between fish-eye and catadioptric camera projections has been discussed in detail by Ying and Hu [22].

Barreto and Araujo [23,24] also describe geometric theory for the central catadioptric projection of lines, and determine the position of the effective viewpoint and the absolute conic in the image plane based on the projection of lines as conic loci. They propose the fitting of conic sections to projected lines. While catadioptric cameras are not proposed for use in this paper, conic sections could be used to determine the vanishing points in place of the circle fitting proposed by this paper. However, occlusion can have a higher impact on the accuracy of conic fitting than it does

on circle fitting [25]. In the case of this paper, it can be seen that the majority of the projected lines are occluded as they extend beyond the image sensor boundaries (it should be noted that advanced methods can be used to improve the accuracy of conic fitting in the presence of occlusion [26]). Circle fitting is also a simpler task than conic fitting due to the decreased number of parameters, and we explicitly demonstrate that circles are an accurate model for lines projected under equidistant distortion (Section 2.3). For these reasons, circle fitting is used in this paper.

2.1. Rectilinear projection

Fig. 1 describes the principles of projection for a simple rectilinear pin-hole camera. The 3D coordinate system has its origin, $\mathbf{O} = [0, 0, 0]^T$, at the focal point (i.e. at the pin-hole), with the z-axis coincident with the optical axis of the camera. The rectilinear image plane is parallel to the xy-plane, with the u - and v -axes parallel to the x - and y -axes, respectively. The inversion inherent in the projection \mathbf{O} through means the u - and v -axes are inverted compared to the x - and y -axes. The rectilinear image plane is positioned a distance f from the xy-plane, where f is the focal length of the pin-hole camera. $\mathbf{P} = [P_x, P_y, P_z]^T$ refers to a point on the line L in 3D space, $\mathbf{p} = [p_u, p_v]^T$ refers to the corresponding projected point on the rectilinear image plane, and θ is the angle the projection line of point \mathbf{P} makes with the z-axis at the origin.

The projection of a point in 3D space to the rectilinear image plane via pin-hole projection is given by [1]:

$$\mathbf{p} = f \begin{bmatrix} P_x/P_z \\ P_y/P_z \end{bmatrix} \quad (1)$$

$$|\mathbf{p}| = f \tan \theta \quad (2)$$

where $|\mathbf{p}|$ can be described as the radial distance from the distortion centre to the projected point \mathbf{p} .

2.1.1. Projection of a line to the rectilinear image plane

A line in 3D space can be described by:

$$\mathbf{P}(t) = \mathbf{D}t + \mathbf{Q} \quad (3)$$

where $\mathbf{D} = [D_x, D_y, D_z]^T$ is the unit direction vector of the line, $\mathbf{Q} = [Q_x, Q_y, Q_z]^T$ is a point through which the line passes and t is the distance parameter that describes any given point on the line. Applying (3) to (1) gives:

$$\mathbf{p}(t) = \begin{bmatrix} D_x t + Q_x \\ D_y t + Q_y \end{bmatrix} \frac{f}{D_z t + Q_z} \quad (4)$$

Rearranging both equations in terms of t , and equating gives:

$$p_v = m p_u + k \quad (5)$$

which is the equation of a straight line in the undistorted image space, where the slope against the u -axis, m , and the v -axis intersection, k , are given by:

$$m = \frac{D_z Q_y - D_y Q_z}{D_z Q_x - D_x Q_z} \quad (6)$$

$$k = \frac{f(D_y Q_x - D_x Q_y)}{D_z Q_x - D_x Q_z}$$

If the projected 3D line intersects the projection centre (i.e. if $\mathbf{Q} = [0, 0, 0]^T$), it can be seen from (4) that the projection degenerates to the point $\mathbf{p} = [D_x/D_z, D_y/D_z]^T$ on the image plane. Intuitively, if the line is also coincident with the z-axis, i.e. when $\mathbf{D} = [0, 0, 1]^T$, the projection degenerates to $\mathbf{p} = [0, 0]^T$, which is a single point at the origin of the image plane axes.

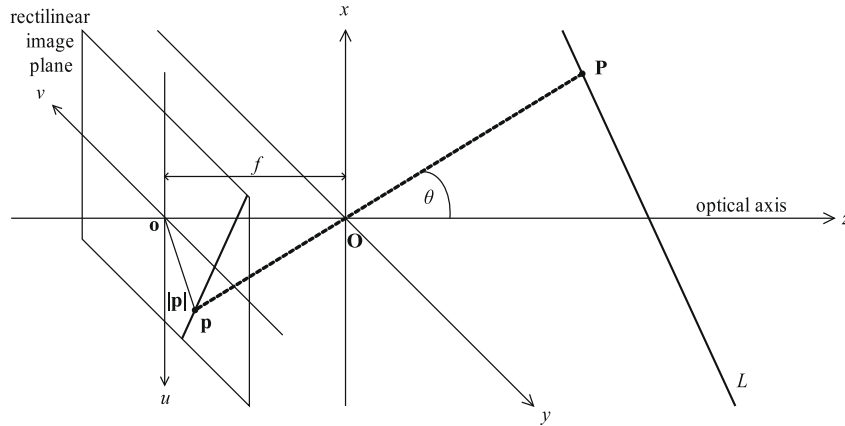


Fig. 1. Rectilinear pin-hole projection.

2.1.2. Vanishing points on the rectilinear image plane

The vanishing point of a projected set of parallel lines is given as the limit of \mathbf{p} as $|t| \rightarrow \infty$. That is:

$$\mathbf{p}_{vp} = \lim_{|t| \rightarrow \infty} \mathbf{p}(t) = \frac{f}{D_z} \begin{bmatrix} D_x \\ D_y \end{bmatrix} \quad (7)$$

Since the limit of \mathbf{p} as $t \rightarrow \infty$ and $t \rightarrow -\infty$ are the same, there is only a single vanishing point for the projection of the set of parallel lines. This is the vanishing point of the projection of any 3D lines parallel to the unit direction vector \mathbf{D} (Fig. 2).

If the 3D lines are parallel to the z -axis ($\mathbf{D} = [0, 0, 1]^T$), then it can be seen from (7) that their vanishing point is $\mathbf{p}_{vp} = [0, 0]^T$. However, if the 3D lines are parallel to the xy -plane ($\mathbf{D} = [D_x, D_y, 0]^T$), then the projected lines will be parallel on the image plane, with the vanishing point \mathbf{p}_{vp} located at ∞ .

2.2. Equidistant fish-eye projection

Fig. 3 describes the principles of equidistant projection for a simple model of an equidistant camera system. Continuing to assume for now that the origin of the equidistant image plane coordinates is located at the distortion centre, the projection of the 3D point \mathbf{P} onto the equidistant image plane is given by $\mathbf{p}' = [p'_u, p'_v]^T$. In Fig. 3, the distortion centre is coincident with the intersection of the optical axis (z -axis) with the image plane (the principal point). However, in real cameras potentially containing numerous optical elements, the principal point and the distortion centre can deviate significantly, as described in detail by [27]. For simplicity, we allow the principal point and the distortion centre to be the same, although the algorithm we describe in Section 3 finds the distortion centre alone.

The radial distance $|\mathbf{p}'|$ from the distortion centre is given by [1]:

$$|\mathbf{p}'| = f\theta \quad (8)$$

The conversion between the undistorted image radial distance and distorted image radial distance described is obtained by solving (8) in terms of θ , and inserting into (2) to obtain:

$$|\mathbf{p}'| = f \tan \frac{|\mathbf{p}'|}{f}, \mathbf{p} = \frac{|\mathbf{p}'|}{|\mathbf{p}|} \mathbf{p}' \quad (9)$$

These equations describe the transform of a point \mathbf{p}' on the distorted equidistant image plane to a point \mathbf{p} on the undistorted rectilinear image plane, where $|\mathbf{p}'|$ is the distorted radial distance of the point \mathbf{p}' from the distortion centre \mathbf{o} , and $|\mathbf{p}|$ is the corresponding undistorted radial distance. The inverse of this conversion is given by:

$$|\mathbf{p}'| = f \arctan \frac{|\mathbf{p}|}{f}, \mathbf{p}' = \frac{|\mathbf{p}'|}{|\mathbf{p}|} \mathbf{p} \quad (10)$$

This describes the conversion from a point on the undistorted rectilinear image plane to the distorted equidistant image plane.

2.2.1. Projection of a line to the equidistant image plane

The projection of a line in 3D space to the distorted equidistant image plane can be determined by applying equidistant distortion to that line when projected to the rectilinear image plane. Thus, if we take (5) as the projection of a straight line on to the rectilinear image plane, and applying distortion using (9), we get the following equation to describe the projection of a 3D straight line on to the distorted image plane:

$$(p'_v - mp'_u) \frac{f}{|\mathbf{p}'|} \tan \left(\frac{|\mathbf{p}'|}{f} \right) - k = 0 \quad (11)$$

where m and k are defined by (6). Alternatively, the parametric form of the equation of the projection of a straight line can be obtained by applying (4) to (10), and thus obtaining:

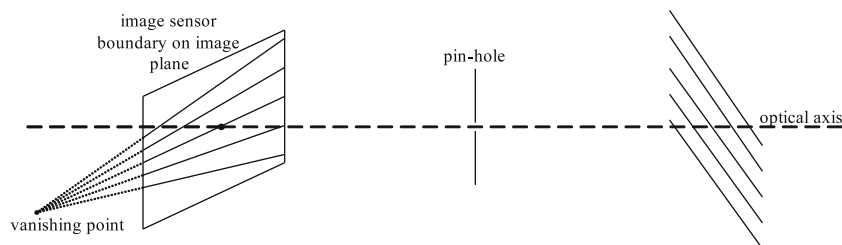


Fig. 2. Projection of parallel lines in a rectilinear pin-hole camera.

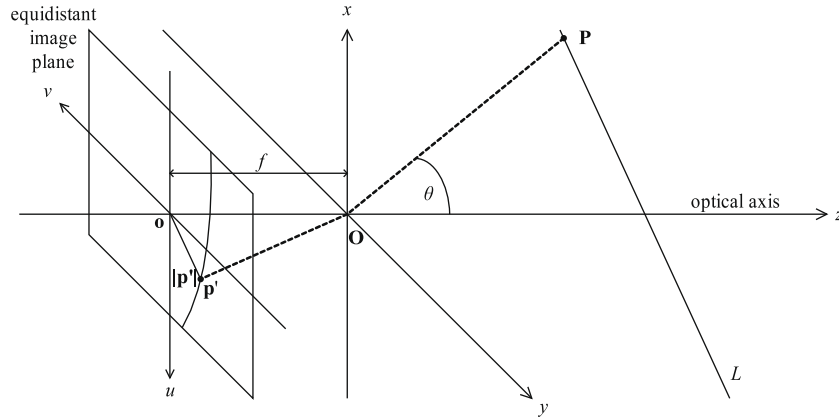


Fig. 3. Equidistant projection.

$$\mathbf{p}'(t) = \begin{bmatrix} D_x t + Q_x \\ D_y t + Q_y \end{bmatrix} \frac{|\mathbf{p}'(t)|}{|\mathbf{p}(t)|} \quad (12)$$

where

$$\frac{|\mathbf{p}'(t)|}{|\mathbf{p}(t)|} = \frac{f \arctan \left(\frac{\sqrt{(D_x t + Q_x)^2 + (D_y t + Q_y)^2}}{D_z t + Q_z} \right)}{\sqrt{(D_x t + Q_x)^2 + (D_y t + Q_y)^2}} \quad (13)$$

This parametric form of the projection of a straight line is more useful when determining the vanishing points in the subsequent sections.

2.2.2. Vanishing points on the equidistant image plane

To find the vanishing point $\mathbf{v}' = [v'_u, v'_v]^T$ of the projection of 3D parallel lines to the distorted image plane, the limit of (12) as $|t| \rightarrow \infty$ is found:

$$\mathbf{v}' = \lim_{|t| \rightarrow \infty} \mathbf{p}'(t) = \begin{bmatrix} D_x \\ D_y \end{bmatrix} \lim_{t \rightarrow \pm \infty} \frac{|\mathbf{p}'(t)|}{|\mathbf{p}(t)|} \quad (14)$$

where

$$\lim_{|t| \rightarrow \infty} \frac{|\mathbf{p}'(t)|}{|\mathbf{p}(t)|} = \frac{f \arctan \left(\frac{\sqrt{D_x^2 + D_y^2}}{D_z} \right)}{\sqrt{D_x^2 + D_y^2}} \quad (15)$$

The projection of an infinitely long 3D line will be a curve that exists in more than one quadrant in the distorted image plane. The exception is when the 3D lines are parallel to the optical axis. In this case, the projection of such lines will intersect the distortion centre, and as such be straight. For any other infinitely long 3D line, the extremities of the projected curve will exist in opposite quadrants. Therefore, the four-quadrant arctangent must be used instead of the standard arctangent function described in (12) and (13). An efficient approximation of the four-quadrant arctangent function is described in [28]. Thus, the two vanishing points are:

$$\mathbf{v}'_1 = \begin{cases} \begin{bmatrix} D_x \\ D_y \end{bmatrix} \frac{f}{\sqrt{D_x^2 + D_y^2}} E, & \phi_{vp} \geq 0 \\ \begin{bmatrix} D_x \\ D_y \end{bmatrix} \frac{f}{\sqrt{D_x^2 + D_y^2}} (-E), & \phi_{vp} < 0 \end{cases} \quad (16)$$

$$\mathbf{v}'_2 = \begin{cases} \begin{bmatrix} D_x \\ D_y \end{bmatrix} \frac{f}{\sqrt{D_x^2 + D_y^2}} (E - \pi), & \phi_{vp} \geq 0 \\ \begin{bmatrix} D_x \\ D_y \end{bmatrix} \frac{f}{\sqrt{D_x^2 + D_y^2}} (\pi - E), & \phi_{vp} < 0 \end{cases} \quad (17)$$

where

$$E = \arctan \left(\frac{\sqrt{D_x^2 + D_y^2}}{D_z} \right) \quad (18)$$

and ϕ_{vp} is the angle the line that intersects the vanishing point and the distortion centre makes with the u -axis, and $-\frac{\pi}{2} < \phi_{vp} \leq \frac{\pi}{2}$.

The vectors denoted as \mathbf{v}'_1 and \mathbf{v}'_2 describe the distorted vanishing points (Fig. 4) of a set of lines parallel to the 3D unit direction vector \mathbf{D} . Both \mathbf{v}'_1 and \mathbf{v}'_2 are constant, dependent only on the unit direction vector \mathbf{D} and the camera focal length f . That is, for any camera with focal length f and any line described by \mathbf{D} and \mathbf{Q} , $f/\sqrt{D_x^2 + D_y^2}$ and E are both constant. If we consider $[D_x, D_y]^T$ as a vector from the distortion centre \mathbf{o} , then we can see that the two vanishing points are simply scaled versions of this vector, that is, the two vanishing points lie in the same (or more typically opposite) directions from \mathbf{o} . As such, the line that joins points \mathbf{v}'_1 and \mathbf{v}'_2 also intersects the distortion centre \mathbf{o} .

If the parallel set of 3D lines is parallel to the xy -plane ($D_z = 0$), the vanishing points become:

$$\mathbf{v}'_1 = \begin{bmatrix} D_x \\ D_y \end{bmatrix} \frac{\pi f}{2\sqrt{D_x^2 + D_y^2}} \quad (19)$$

$$\mathbf{v}'_2 = \begin{bmatrix} D_x \\ D_y \end{bmatrix} \frac{-\pi f}{2\sqrt{D_x^2 + D_y^2}} \quad (20)$$

If the parallel set of 3D lines are also parallel to the z -axis ($D_x = D_y = 0$), the vanishing points become:

$$\mathbf{v}'_1 = \mathbf{v}'_2 = \begin{bmatrix} 0 \\ 0 \end{bmatrix} \quad (21)$$

Thus, there is only a single vanishing point for lines parallel to the z -axis, which is coincident with the distortion centre, as illustrated in Fig. 5.

2.3. Estimating the equidistant projection of straight lines as circles for practical implementation

Eqs. (12) that describe the equidistant projection of straight lines are relatively complex, and attempting to fit image data to these equations could prove both costly and complex. It would be far more desirable if projected lines could be fit to some simpler geometric shape. Strand and Hayman [29], Barreto and Daniilidis [30] and Bräuer-Burchardt and Voss [8] suggest that the projection of straight lines in cameras exhibiting radial distortion results in circles on the image plane. Bräuer-Burchardt and Voss [8], in contrast to the other two [29,30], explicitly use fish-eye images in their examples. However, all three methods assume that the

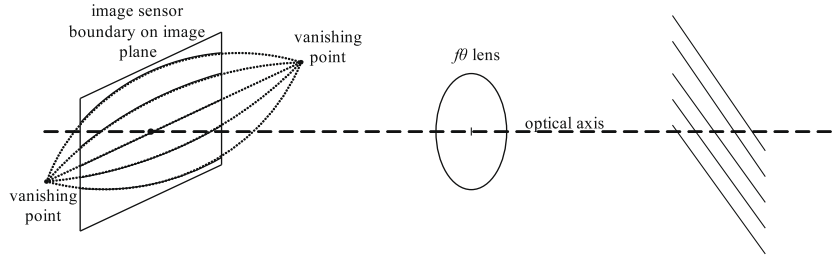


Fig. 4. Projection of parallel lines in an equidistant fish-eye camera.

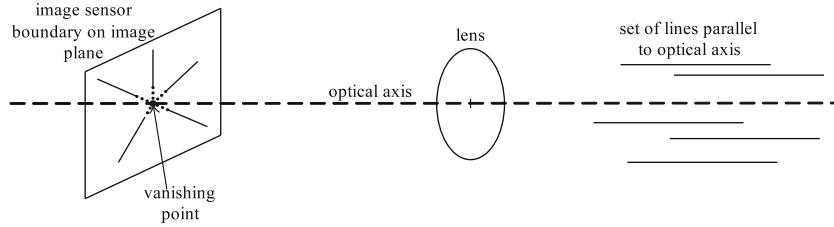


Fig. 5. Projection of parallel lines that are also parallel to the optical axis in both pin-hole and f/θ lensed cameras. The single vanishing point is coincident with the distortion centre.

camera system follows the division model of radial distortion, and this model is also used for the basis of the method described in this paper. Tardif et al. [31] also use the division model with both fish-eye and paracatadioptric cameras displaying high levels of distortion, with calibration being done by iteratively and alternately fixing and computing the distortion centre and distortion function until convergence is observed.

If circles can be used to estimate the projection of a straight line on to the equidistant image plane, the method of fitting a function to the data are simpler. Up until now, we have assumed that the origin of the image plane is at the distortion centre. Of course, that is not practical, as the distortion centre may not be known and therefore cannot be used as the origin of the image coordinate system. With the origin and distortion centre not co-located, (11) becomes:

$$(p'_v - mp'_u) \frac{f}{d} \tan\left(\frac{d}{f}\right) - k = 0 \quad (22)$$

where

$$d = \sqrt{(p'_u - o_u)^2 + (p'_v - o_v)^2} \quad (23)$$

where $[o_u, o_v]^T$ is the distortion centre. Thus, to fit data to this function, there are five parameters that need to be estimated by a data fit algorithm. In contrast, a circle fit algorithm requires the estimation of only three parameters (the centre point coordinates and the radius). Additionally, in practical applications where fish-eye lenses are used, e.g. automotive camera systems, the calibration and compensation will typically be performed using embedded systems, and as such the presence of the tan function in (22) is undesirable. Thus in this section, in order to reduce complexity, we aim to show that the division model can be used as an accurate model of the equidistant distortion function, and thus that circles can be used to accurately estimate the projection of a straight line on to the equidistant image plane.

2.3.1. Estimating equidistant distortion using the division model

The first order form of the division model, i.e. the form of the model that can be used with circle fitting, was introduced almost simultaneously, and apparently independently, by Bräuer-Burhardt and Voss [8] and Fitzgibbon [9]. Bräuer-Burhardt and Voss

had previously published a second order form of the model [32] a year earlier. The first order division model can be described as:

$$|\mathbf{p}| = \frac{s|\mathbf{q}'|}{1 - \lambda|\mathbf{q}'|^2}, \quad \mathbf{p} = \frac{|\mathbf{p}|}{|\mathbf{q}'|} \mathbf{q}' \quad (24)$$

and the inverse is:

$$|\mathbf{q}'| = |\mathbf{p}| \frac{\sqrt{s + 4\lambda|\mathbf{p}|^2} - s}{2\lambda|\mathbf{p}|^2}, \quad \mathbf{q}' = \frac{|\mathbf{q}'|}{|\mathbf{p}|} \mathbf{p} \quad (25)$$

where $\mathbf{q}' = [q'_u, q'_v]^T$ is the distorted version of \mathbf{p} under the division model of radial distortion, λ is the distortion coefficient, and s is an additional scaling factor inserted to ensure that the focal length of an image rectified using the division model is equal to the focal length of the equivalent equidistant distorted image.

Fitzgibbon [9] provides empirical validation of the division model, comparing it and the odd-order polynomial model to the true distortion curve of a camera. However, they failed to extend this validation to the case of the highly non-linear fish-eye distortion curves. This is what we aim to do in this section. The accuracy of using the division model as a means to estimate the projection of lines in equidistant fish-eye cameras depends entirely on the ability of (24) to model the equidistant radial distortion curve, described by (9).

Fig. 6a shows the fit of this division model to a modelled distortion curve of a camera with a 179° field-of-view,¹ normalised to the equidistant distorted image circle radius $|\mathbf{p}'|_{\max}$. It can be seen from the figure that the fitted curve and the distortion curve are practically essentially congruent. The distortion curve is normalised to make it independent of internal camera parameters (e.g. sensor size and focal length). Thus, the normalised focal length f can be determined, from (8):

$$f = \frac{|\mathbf{p}'|_{\max}}{\theta_{\max} |\mathbf{p}'|_{\max}} = \frac{1}{\theta_{\max}} \quad (26)$$

¹ The effect of attempting to rectify cameras with a field-of-view of larger than 180° is discussed in [31]. Two points in the original image can be mapped to a single point in the rectified image, and 3D points with an incident angle of 90° are mapped to points at infinity. Thus, we will only examine the distortion curves of cameras with fields-of-view strictly smaller than 180°.

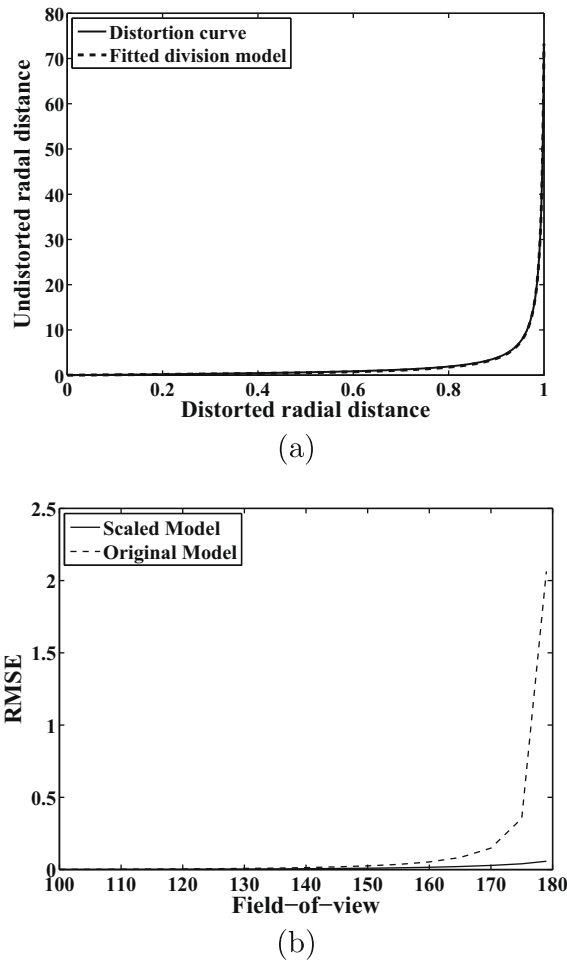


Fig. 6. (a) Nonlinear least squares fit of the scaled division model to the distortion curve (from 0° to 179°). (b) Root means square error of fit of the division model to the distortion curve for varying fields-of-view (in degrees). The solid line shows the error in using the scaled division model and, for comparison, the dashed line shows the error in using the division model with no scaling.

where θ_{\max} is the maximum incident ray angle for the modelled camera (one half of the field-of-view). The normalisation makes $|\mathbf{p}'|_{\max} = 1$.

The fit is done using `cftool` function in the MATLAB Curve Fitting Toolbox. In this example, fitting (24) to the distortion curve returned a root mean square error (RMSE) of 0.057. Fig. 6b shows the error of fit of the scaled division model to the modelled distortion curves for equidistant cameras with various fields-of-view. It can be seen that the error remains very small even for high levels of distortion.

Thus, it can be said for an appropriately chosen distortion parameter λ , the distorted radial distance under the division model distortion is approximately equal to the distorted radial distance under equidistant projection:

$$|\mathbf{q}'| \approx |\mathbf{p}'|, \mathbf{q}' \approx \mathbf{p}' \quad (27)$$

2.3.2. The projection of a line under the scaled division model

It has already been shown that the projection of a 3D straight line for the original division model in [29,30] is a circle, but we will show here for completeness that this holds also for the scaled division model. Taking the equation of a line in undistorted image space as given in (5), distorting it by applying (24) and reformulating, gives:

$$k\lambda(q'_u 2 + q'_v 2) + msq'_u - sq'_v + k = 0 \quad (28)$$

where m and k are defined in (6). This equation is in the general form of a circle.

It is therefore the assertion of this paper that the scaled division model (24) can be used to accurately model the distortion introduced by equidistant camera systems, and thus, straight lines in 3D space can be accurately described as circles under equidistant projection.

2.3.3. Vanishing points under the division model

Applying the parametric form of the projection of a 3D line in rectilinear space (4) to the scaled division model distortion (25) gives the two parametric equations that describe the projection of a straight line in 3D space to the distorted space, under the division model of radial distortion:

$$\mathbf{q}'(t) = \begin{bmatrix} D_x t + Q_x \\ D_y t + Q_y \end{bmatrix} F(t) \quad (29)$$

where

$$F(t) = \frac{\left(\sqrt{s + 4\lambda \frac{f^2(D_x t + Q_x)^2 + f^2(D_y t + Q_y)^2}{(D_x t + Q_x)^2}} - s \right)}{2\lambda \left(\frac{(D_x t + Q_x)^2 + (D_y t + Q_y)^2}{D_x t + Q_x} \right)} \quad (30)$$

Again, the vanishing points $\mathbf{w}' = [w'_u, w'_v]^T$ are found as the limit of $\mathbf{q}'(t)$ as $|t| \rightarrow \infty$. The first vanishing point is calculated by taking the positive of the square roots in (29), and the second is obtained by taking the negative of the square roots:

$$\mathbf{w}'_1 = \lim_{|t| \rightarrow \infty} \mathbf{q}'(t)_{\sqrt{+}} = \begin{bmatrix} D_x \\ D_y \end{bmatrix} \lim_{|t| \rightarrow \infty} F(t)_{\sqrt{+}} \quad (31)$$

$$\mathbf{w}'_2 = \lim_{|t| \rightarrow \infty} \mathbf{q}'(t)_{\sqrt{-}} = \begin{bmatrix} D_x \\ D_y \end{bmatrix} \lim_{|t| \rightarrow \infty} F(t)_{\sqrt{-}} \quad (32)$$

where

$$\lim_{|t| \rightarrow \infty} F(t)_{\sqrt{\pm}} = \frac{(\pm \sqrt{sD_z^2 + 4\lambda f^2 D_y^2 + 4\lambda f^2 D_x^2 - sD_z})}{2\lambda (D_x^2 + D_y^2)} \quad (33)$$

Additionally, both \mathbf{w}'_1 and \mathbf{w}'_2 are scaled versions of the vector $[D_x, D_y]^T$, and as such, the line that joins points \mathbf{w}'_1 and \mathbf{w}'_2 also intersects the distortion centre. The following section discusses how this can be used to estimate the location of the distortion centre.

3. Application in distortion centre estimation

In the previous section, we have shown how the equidistant projection of 3D straight lines can be approximated as arcs of circles, and that a set of projected parallel 3D lines converge at two vanishing points on the image plane. We have also shown that the line that intersects these two vanishing points also intersects the distortion centre. Using these principles, in this section we shall demonstrate how the distortion centre can be estimated.

The basic principle of the proposed method is as follows. The method involves the use of a calibration rig, consisting of a planar diagram with known geometric properties in 3D space. In particular, this diagram consists of a set of parallel lines. An image is captured of the parallel lines pattern, and the pattern is rotated and captured again, as shown in Fig. 7a and b.

Thus we have two pairs of parallel lines in 3D space, which when imaged can be approximated as two sets of circular arcs. These arcs in the image are extracted using an appropriate method (in this case, we used Sobel edge detection). The edges are labelled,

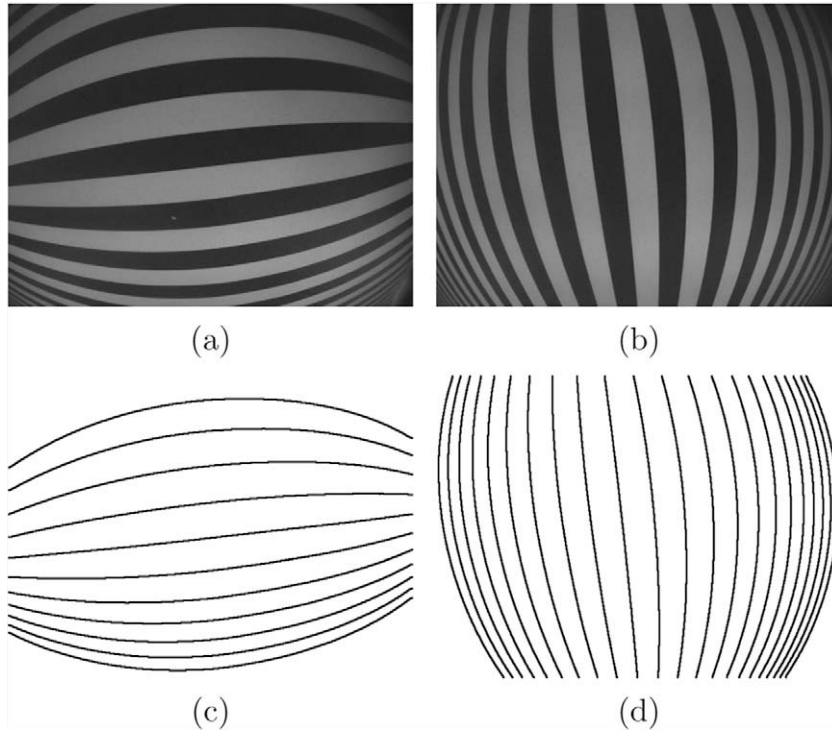


Fig. 7. (a) and (b) Calibration diagrams captured using an equidistant fish-eye camera. (c) and (d) Edges extracted from the calibration images.

ignoring any edges that are less than 90% of the width or height of the image (depending on the direction of the lines in the image), such that only edges that span the entire image are used, and partial edges (such as those in the corners of Fig. 7a and b) are ignored. Fig. 7c and d shows the extracted edges.

3.1. Distortion centre estimation

3.1.1. Estimating the vanishing points

Schaffalitzky and Zisserman [33] describe how the vanishing point for a non-distorted set of rectilinear projected concurrent lines can be estimated using Maximum Likelihood Estimation (MLE), to provide a set of corrected lines that are exactly concurrent. The method described can be extended to support arcs of circles, and two vanishing points, rather than straight lines and single vanishing points. In this case, the model consists of two vanishing points. For each pair of lines, circles are fit to the projected lines, and their intersection points are determined (their putative vanishing points). The support of each edge in the image for the putative vanishing points is found by the LMS fitting of circles through the edge points, and forcing the fitted circle through the vanishing point pair, by minimising the error function:

$$\mathfrak{F}_1 = \sum_{i=1}^N \left((u_i - u_0)^2 + (v_i - v_0)^2 - R^2 \right)^2 \quad (34)$$

where $[u_i, v_i]^T$ are the points on the distorted line, N is the number of sampled points on that distorted line, $[u_0, v_0]^T$ is the centre and R is the radius of the fitted circle. Clearly, the lower the returned error, the more support a given edge has for the putative vanishing point pair.

Schaffalitzky and Zisserman suggest using a threshold to determine if an edge supports a particular putative vanishing point, as is standard with RANSAC algorithms [34, p. 118]. However, we prefer to simply select the vanishing point pair that returns the minimum error across all edges in the image. Once a model with maximum

support is obtained, the MLE of the vanishing point pair is computed using a non-linear optimisation algorithm such as Levenberg-Marquardt [35]. That is, the error function is minimised for the entire image:

$$\mathfrak{F}_2 = \sum_{j=1}^M \sum_{i=1}^N \left((u_{j,i} - u_{0j})^2 + (v_{j,i} - v_{0j})^2 - R_j^2 \right)^2 \quad (35)$$

where M is the number of edges in the image. In the optimisation of the vanishing points, a relaxation technique of alternation type is employed, whereby each vanishing point is alternately fixed and the other is updated:

- (1) Obtain the putative vanishing points.
- (2) Fix the vanishing point \mathbf{w}'_1 and update the opposite vanishing point \mathbf{w}'_2 such that (35) is minimised for the chosen vanishing point locations.
- (3) Fix \mathbf{w}'_2 and update \mathbf{w}'_1 .
- (4) Repeat steps 2 and 3 until convergence is observed and (35) is minimised for both vanishing points.

In each iteration, the circles can be parameterised by the vanishing points and another arbitrary point per edge. If we fix one coordinate of the third point, in each iteration of the steps above (i.e. when two candidate vanishing points have been chosen), the minimisation of the circle fit errors becomes a single parameter per edge. For example, when fitting the circles through the vanishing points to the vertical edges, we fix the u -coordinate of the third point at the horizontal axis of the image, and optimise the v -coordinate such that the error (34) is minimised. For the horizontal edges, the v -coordinate is fixed at the vertical axis.

Thus, the MLE of the vanishing points is found by determining a set of circles on the image plane that are convergent on the vanishing points, corresponding to a set of concurrent 3D lines, such that the distance of the circles to the sampled edge points is minimised. This is repeated for both the vertical and horizontal sets of curves,

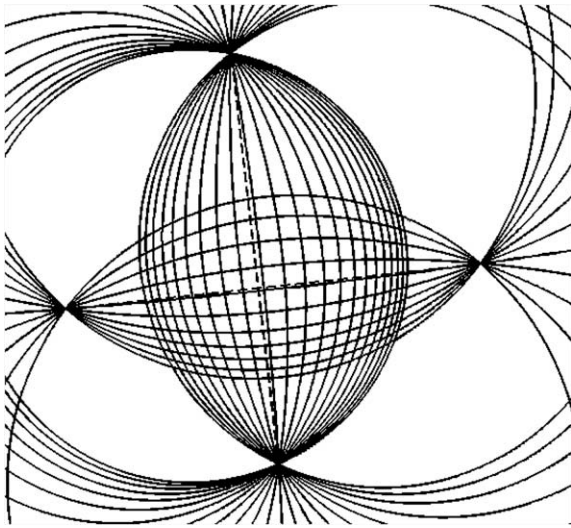


Fig. 8. The circles fitted to the extracted edges. The vanishing points are the points of intersection of the circles. The lines intersecting the vanishing points are shown as dashed lines.

to determine the two pairs of vanishing points. Fig. 8 shows the two sets of fitted circles with the MLE determined vanishing points.

In this method, there is no voting to remove outlier. Thus, this is not a true RANSAC method. A RANSAC algorithm is not necessary, as there should be no outliers in the data due to non-convergent edges, i.e. it is known that all edges in the image are co-planar, will converge at two vanishing point and will fit to circles, as a calibration diagram consisting of straight line (which project to circles) is used. The errors that occur are due only to noise in the image.

However, the method of determining the putative vanishing point pair with minimum error is useful for obtaining an initial estimate for the non-linear optimisation.

3.1.2. Estimating the distortion centre

The estimation of the vanishing points in the previous section via minimisation of the error of circle fits to the data are applied to both of the calibration images, as shown in Fig. 8. From each of the calibration images, a line can be created as the line that joins the two vanishing points. As was demonstrated in Section 2.3.3, these lines both intersect the distortion centre. Therefore, the distortion centre can be estimated as the point at which the two lines cross.

3.2. Evaluation of estimation using synthetic images

In order to test the accuracy of utilising fish-eye perspective in the estimation of the distortion centre, we created a set of synthetic images with varying known distortion centres and various simulated image imperfections (radial distortion, noise and sharpness) and environmental imperfections (imperfect illumination and misalignment of the test diagram) to create a range of real-world image conditions. We then calculated the estimated distortion centre and compared it with the known actual distortion centre to determine the accuracy of the estimation algorithm.

1. *Rotation transformations:* The rotation transformations are performed on the test diagram image to model the fact that the test diagram may not be aligned exactly perpendicular to the principal axis of the camera. More accurately, the rotation transformations model the rotation of the camera about each of the x -, y - and z -axes. This is equivalent, however, to rotating the test diagram about the x -, y - and z -axes. The perspective and rotation transforms are described in detail in [36]. Rotation about the x -axis by angle θ is determined by the transformations:

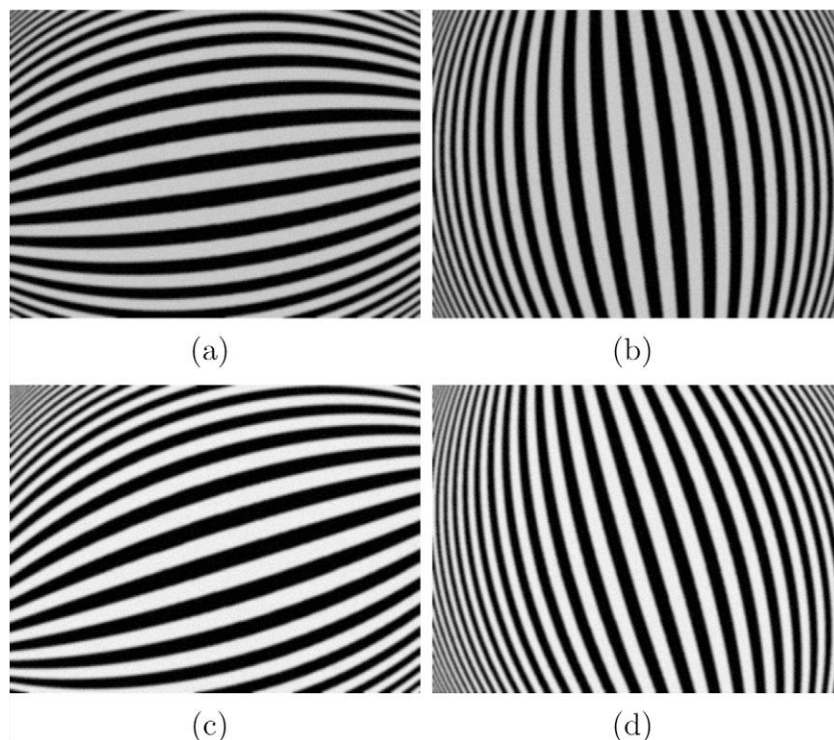


Fig. 9. Sample set of synthetic calibration image pairs.

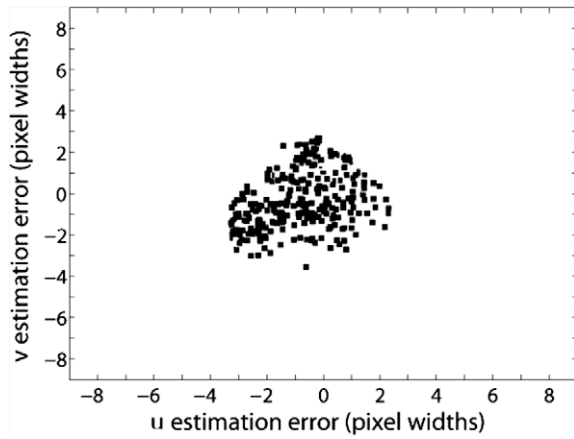


Fig. 10. Distribution of the synthetic image results as distance of the estimated distortion centre from the modelled distortion centre.

$$u_\theta = \frac{f(u - u_0)}{f \cos \theta + (v - v_0) \sin \theta} \quad (36)$$

$$v_\theta = f \frac{(v - v_0) \cos \theta - f \sin \theta}{f \cos \theta + (v - v_0) \sin \theta} \quad (37)$$

where $[u, v]^T$ is the original image point, $[u_\theta, v_\theta]^T$ is the transformed image point, $[u_0, v_0]^T$ is the point of rotation, and f is the effective focal length of the camera. Similarly, rotation about the y -axis by ϕ is determined by:

$$u_\phi = f \frac{(u - u_0) \cos \phi - f \sin \phi}{f \cos \phi + (u - u_0) \sin \phi} \quad (38)$$

$$v_\phi = \frac{f(v - v_0)}{f \cos \phi + (u - u_0) \sin \phi} \quad (39)$$

Finally, rotation about the z -axis by angle α :

$$u_\alpha = (u - u_0) \cos \alpha - (v - v_0) \sin \alpha \quad (40)$$

$$v_\alpha = (u - u_0) \sin \alpha + (v - v_0) \cos \alpha \quad (41)$$

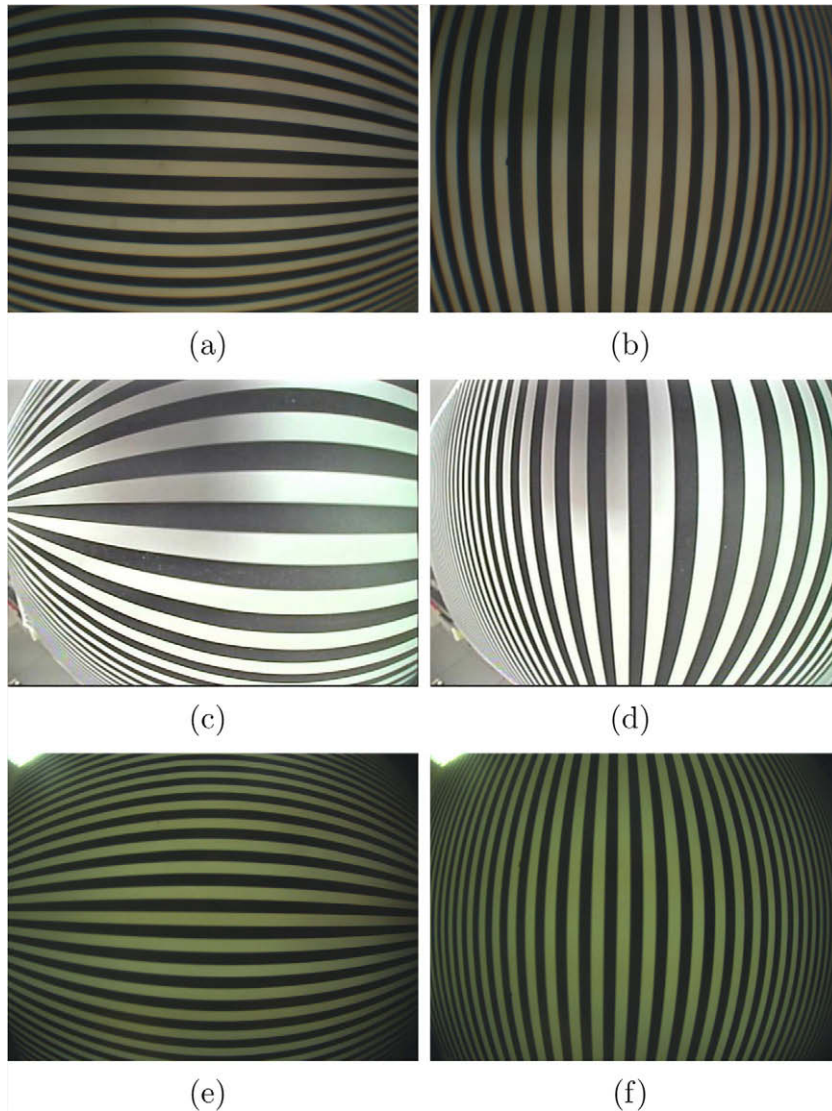


Fig. 11. Sample calibration image pairs: (a) and (b) 122° field of view wide-angle camera, (c) and (d) 162° field of view wide-angle camera, and (e) and (f) 170° field of view fish-eye camera.

When creating the synthetic images, θ , ϕ and α were set randomly to between -20° and $+20^\circ$. For larger angles of rotation, there is the potential for a drop in the quality of circle fitting. The vanishing points can become mapped to within the image sensor boundary, which results in greater occlusion of the projected curves, and a reduced number of sample points, with the associated decrease in the accuracy of the circle fitting.

2. Radial distortion: Radial distortion is added to the image using the equidistant distortion function described in (9). For the synthetic image creation, f was randomly set at between 255 and 380 pixel widths (180° and 120° fields-of-view, respectively), which models wide-angle to strong fish-eye lenses. The applied radial distortion was centred on distortion centre that was allowed to be within 96 pixel widths of the image centre. Hartley and Kang [27] tested several cameras and measured that the distortion centres were up to 30 pixel widths from the image centre in a 640×480 image. Our measurements on real cameras gave similar results.

3. Edge sharpness: All cameras will have an inherent *Modulation Transfer Function* (MTF) that causes a reduction in sharpness of the image, essentially “blurring” the images. In digital photography, factors affecting MTF include aberrations in the optics of the camera, diffraction effects and leakage of photocurrent between pixels in the image sensor. However, this blurring can generally be modelled as a Gaussian smoothing filter applied to the ideal image [37]. We measured the standard deviations of Gaussian low-pass filter unit step responses that approximate the edge profiles of several cameras ranging from high-end to low-end consumer cameras (including the Canon EOS 10D, the Sony DSC-H2 with wide-angle lens attachment, the Minolta Dimage Z6 with fish-eye lens attachment and the Nikon Coolpix P2), as well as two OEM evaluation modules (the Micron MI-0343 and the Omnivision OV7710 with fish-eye lens). We found that the measured standard deviation was between $\sigma = 0.474$ and $\sigma = 1.2$ pixel widths for 640×480 images. For our synthetic image creation, we used a standard deviation of $\sigma = 2$ pixel widths.

4. Other modelling considerations: Several other camera conditions were modelled:

- **Pixel aspect ratio:** The pixel aspect ratio is 1:1 (i.e. pixel width is the same as pixel height).
- **Intensity range:** The synthetic images are single channel images (i.e. greyscale) with a range of 0–1.
- **Illumination of test diagram:** We modelled imperfect lighting conditions and image sensor response, which results in the black and white levels in an image being shifted from the ideal values of 0 (black) and 1 (white) to l_0 and l_1 , respectively. For the purposes of the synthetic image creation, l_0 was set to between 0 and 0.2 randomly, and l_1 to between 0.7 and 1.0.
- **Noise:** We introduce noise with an image Signal to Noise Ratio (SNR) of 25 dB (as a comparison, the SNR of a VHS video tape is approximately 50dB [3]).

To determine the accuracy of the distortion centre estimation, we created a set of 300 synthetic calibration image pairs with sample resolution of 640×480 pixels, using the methods described above. A subset of these synthetic calibration image pairs is shown in Fig. 9.

For each of the images, the distortion centre was estimated using the method outlined in Section 3.1. The error is calculated as the difference between the known modelled distortion centre $[u_{0,kn}, v_{0,kn}]^T$ and the estimated distortion centre $[u_{0,est}, v_{0,est}]^T$:

$$\epsilon = \sqrt{(u_{0,kn} - u_{0,est})^2 + (v_{0,kn} - v_{0,est})^2} \quad (42)$$

For the set of 300 synthetic images, the average error ϵ_{mean} was 2.77 pixel widths. Fig. 10 shows the distribution of the u and v estimation.

3.3. Evaluation of estimation using with real images

We examine the accuracy of the distortion centre estimation using a set of real calibration image pairs taken using three different wide-angle cameras that adhere to the equidistant mapping function. Samples of the image pairs are shown in Fig. 11. In total, 15 calibration image pairs were taken using each camera (a total of 45 image pairs). Fig. 12 shows the distribution of the distortion

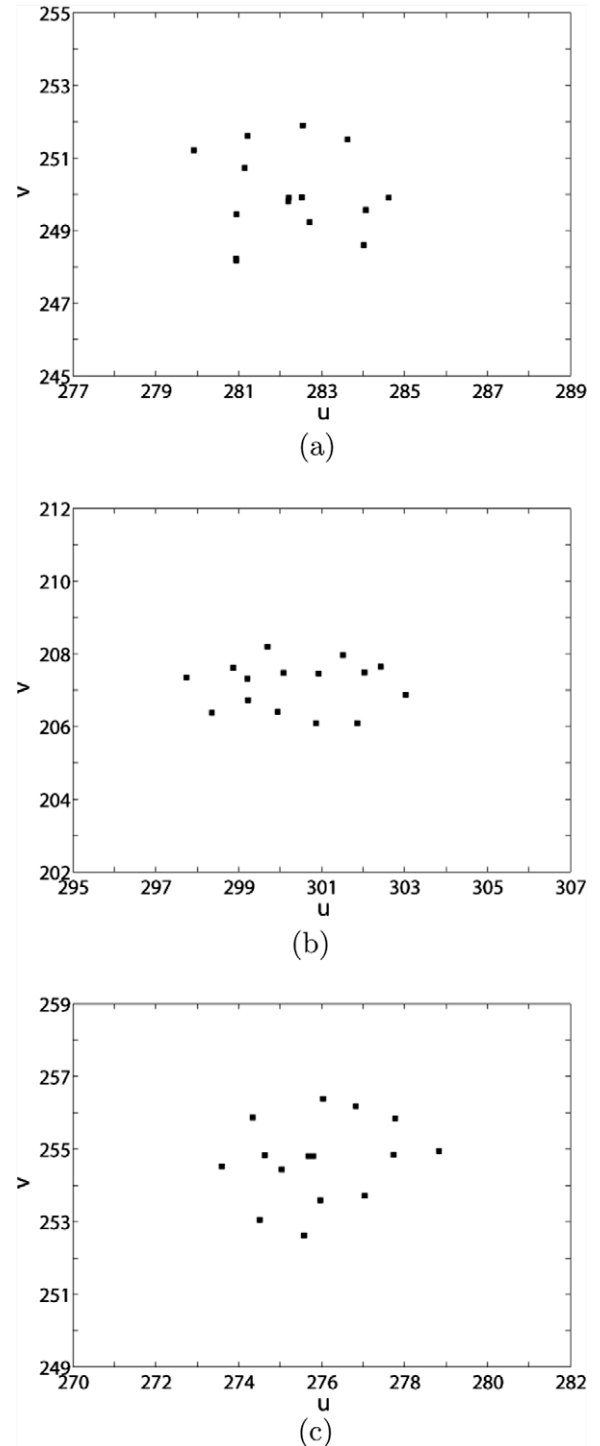


Fig. 12. Distributions of distortion centre estimation: (a) 122° field of view wide-angle camera, (b) 162° field of view wide-angle camera, and (c) 170° field of view fish-eye camera.

centre estimations for each of the cameras. Unlike the synthetically created calibration images, the distortion centre for the cameras used in obtaining the results in this section is unknown. Thus, the estimated distortion centre distribution spread is primarily used in this section to evaluate the distortion centre estimation.

3.4. Stability with lessening radial distortion

Up until now, cases where there is significant radial distortion have been examined. However, it is clear that the algorithm will fail when there is no radial distortion, as this will result in straight lines in the 3D scene being projected to straight lines on the image plane, which will only converge at a single vanishing point. It is natural, however, to wonder what the effect on the distribution of distortion centre estimations will be in the presence of lessening degrees of radial distortion. It is intuitive to assume that the stability of the algorithm will decrease with decreased radial distortion.

In Fig. 13, three cameras are examined. The first is a camera with a field-of-view of 85° , displaying considerable distortion (though not as much as those in Fig. 11). The second is a 54° field-of-view camera displaying considerably less distortion, and the third is a 44° field-of-view camera with relatively small levels of distortion. It can be seen from Fig. 13 that, with decreasing field-of-view and thus decreasing radial distortion, the variance of the distributions of distortion centre estimations increases significantly, which indicates, as expected, that the stability decreases with decreasing field-of-view.

4. Discussion

In this section we have demonstrated how the distortion centre can be estimated using the principles of equidistant fish-eye perspective described in Section 2. Comparing the accuracy of our method with the results given by Hartley and Kang in [27], the distributions of our single calibration image pair distortion centre estimation is significantly smaller than the distribution presented by Hartley and Kang for single calibration images, for both our tests on synthetic and real cameras. In fact, our distributions of estimated centres of distortion for single calibration image pair is of a similar range to the “10 of 19” averaging sets that Hartley and Kang presented.

As a comparison, we have implemented a “5 of 15” averaging of our distortion centre estimation results for each of the cameras presented, whereby we create 100 sets of five randomly chosen images out of the 15 calibration images, and average the distortion centre estimation results. The result is 100 averaged distortion centre estimations. Fig. 14 shows the distribution of this “5 of 15” averaging, as well as a “10 of 15” averaging. The results show that the range of the distributions for both our “5 of 15” and our “10 of 15” averaging is significantly smaller than the equivalent averaging sets Hartley and Kang presented.

The results suggest that our proposed method is more accurate than that presented by Hartley and Kang. Particularly, we get very low deviation in the distributions when averaging is used. However, it is our experience that for most applications, the accuracy

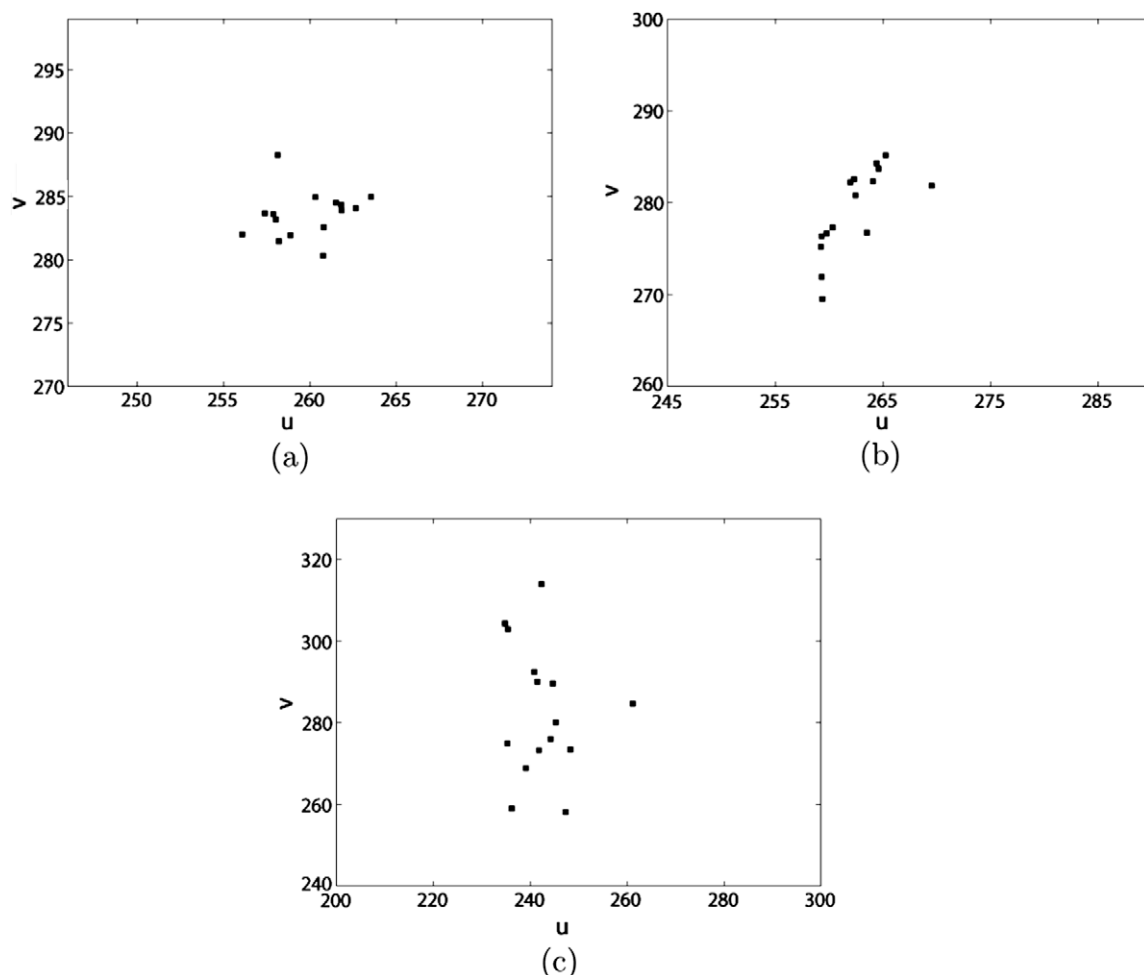


Fig. 13. Distributions of distortion centre estimation: (a) 85° field of view wide-angle camera, (b) 64° field of view wide-angle camera, and (c) 44° field of view fish-eye camera. Notice the changes in scale in each figure.

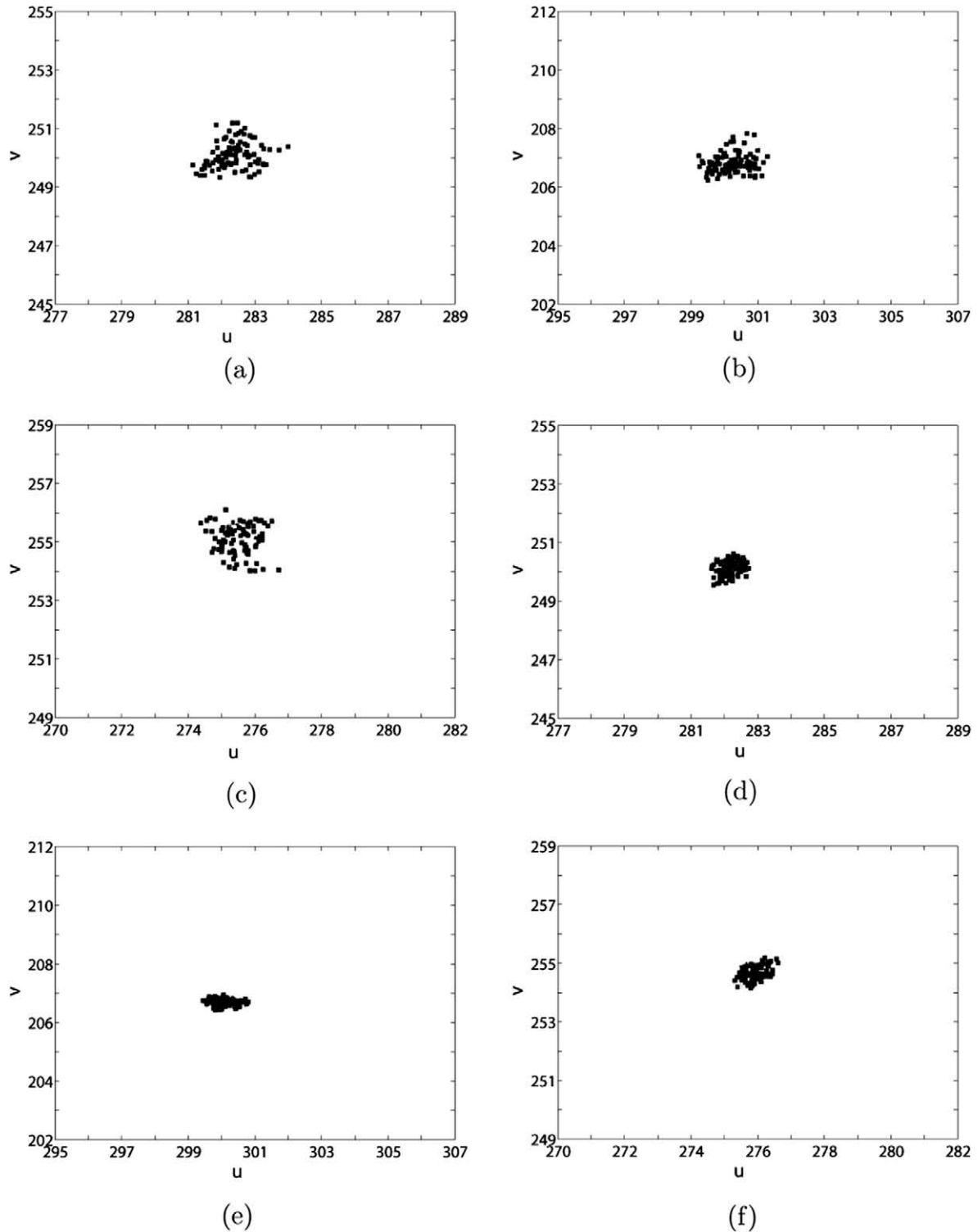


Fig. 14. Distributions of distortion centre estimations. (a)–(c) Using 100 averages of random sets of five images chosen from 15 (i.e. “5 of 15”) for the 122°, 162° and 170° field of view cameras, respectively. (d)–(f) Using 100 averages of random sets of 10 images chosen from 15 (i.e. “10 of 15”) for the same cameras.

of our single pass algorithm should be satisfactory. It should be noted that Hartley and Kang’s method using a 3D calibration pattern can be used to calibrate a camera’s intrinsic and extrinsic (pose) parameters, which is not proposed in this paper.

In Fig. 15, we examine the effect of the selection of an accurate distortion centre on the rectilinearisation of images exhibiting large degrees of radial distortion. The images were corrected using

(10), with an appropriately selected value for f . Visually, it can be seen that the accurate selection of the distortion centre leads to improved rectilinearisation of the distorted images. The correct value for f was chosen using a simple iterative method. For each camera, using a calibration diagram (for example, those in Fig. 11), a range of values of f were iterated. The value for f that displayed the highest rectilinearity on rectification was selected as the

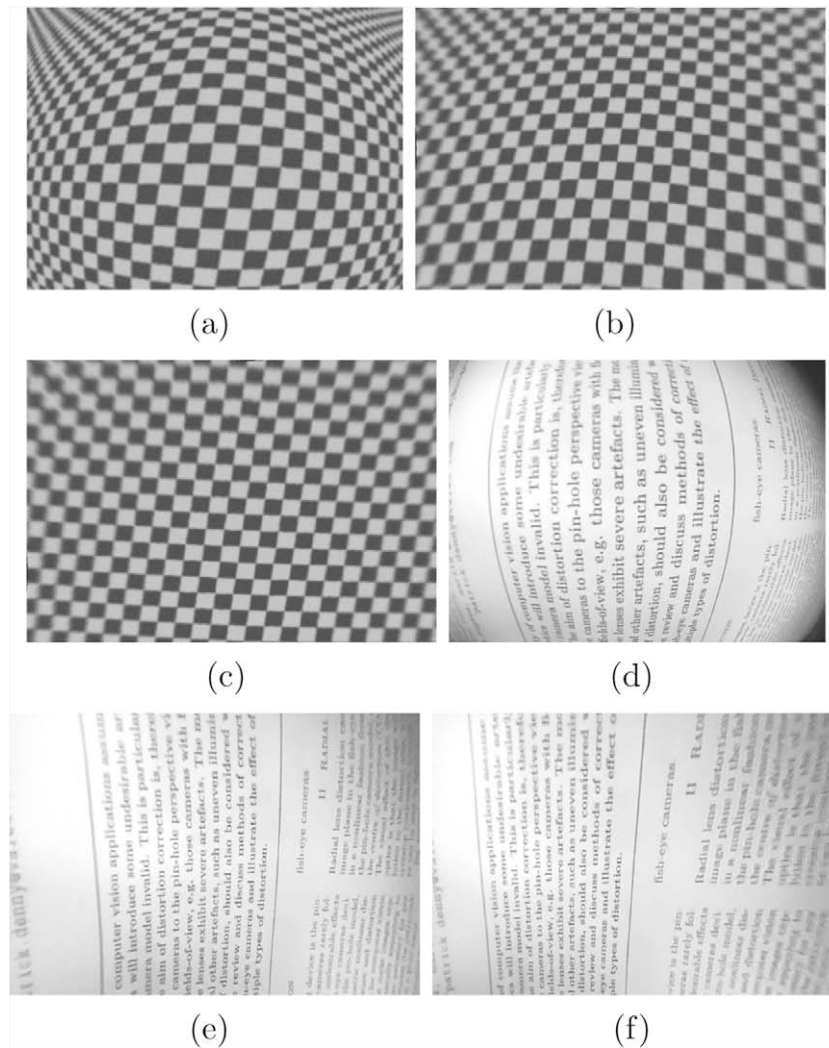


Fig. 15. The effect of accurate distortion centre estimation on radial distortion correction. (a) Synthetically created checkerboard image, (b) corrected using the centre of the image as the distortion centre, and (c) corrected using the centre of distortion estimated at $[326.1, 333.5]^T$. (d) Image captured using the 170° field of view camera, (e) corrected using the centre of the image as the distortion centre, and (f) corrected using the estimated distortion centre $[254.8, 275.1]^T$.

correct value. Rectilinearity was measured by applying a least-mean-square line fit to each edge in the image, and averaging the error for all edges. The rectified image that returned the minimum error displayed the highest rectilinearity.

5. Conclusions

In this paper, we have described the equidistant fish-eye perspective in terms of the projection of sets of parallel lines to the equidistant fish-eye plane. We have shown that a set of 3D parallel lines converge at two vanishing points on the equidistant image plane, in a manner similar to converging at a single point in the rectilinear image plane. The line that intersects these two vanishing points also intersects the distortion centre. We have also demonstrated that, on examination of the accuracy of the division model of radial distortion, circles can be accurately used to describe the projection of straight lines in 3D space to the equidistant image plane.

As an application of the equidistant fish-eye perspective, we have described a method of estimating the distortion centre of an equidistant fish-eye camera, using circle-fitting to extract the 3D parallel lines from the fish-eye calibration diagram, thus determining the vanishing points. We demonstrated the accuracy of this

approach by estimating the distortion centre of a large set of synthetic calibration images, and a smaller set of real calibration images.

Some previous work has been done on orthographic projection perspective [20]. Further work could be done on the perspective of other types of fish-eye projections, such as equisolid or stereographic projections [38]. Additionally, in this paper we have concentrated on the projection of straight lines, as they are a common geometric shape used in camera calibration and the projected lines can be accurately approximated using circles. However, using similar principles, other geometric shapes could be described under the same equidistant projection.

Acknowledgements

This research is funded by Enterprise Ireland and Valeo Vision Systems (formerly Connaught Electronics Ltd.) under the Enterprise Ireland Innovation Partnerships Scheme.

References

- [1] C. Slama (Ed.), *Manual of Photogrammetry*, fourth ed., American Society of Photogrammetry, 1980.

- [2] R. Tsai, A versatile camera calibration technique for high-accuracy 3D machine vision metrology using off-the-shelf TV cameras and lenses, *IEEE Transactions on Robotics and Automation* 3 (4) (1987) 323–344.
- [3] F. Devernay, O. Faugeras, Automatic calibration and removal of distortion from scenes of structured environments, in: *Proceedings of the SPIE Investigative and Trial Image Processing Conference*, vol. 2567, 1995, pp. 62–72.
- [4] J. Perš, S. Kovacic, Nonparametric, model-based radial lens distortion correction using tilted camera assumption, in: *Proceedings of the PRIPG Computer Vision Winter Workshop*, 2002, pp. 286–295.
- [5] M. Ahmed, A. Farag, Nonmetric calibration of camera lens distortion: differential methods and robust estimation, *IEEE Transactions on Image Processing* 14 (8) (2005) 1215–1230.
- [6] A. Basu, S. Licardie, Alternative models for fish-eye lenses, *Pattern Recognition Letters* 16 (4) (1995) 433–441.
- [7] F. Devernay, O. Faugeras, Straight lines have to be straight: automatic calibration and removal of distortion from scenes of structured environments, *International Journal of Machine Vision and Applications* 13 (1) (2001) 14–24.
- [8] C. Bräuer-Burchardt, K. Voss, A new algorithm to correct fish-eye- and strong wide-angle-lens-distortion from single images, in: *Proceedings of the IEEE International Conference on Image Processing*, vol. 1, 2001, pp. 225–228.
- [9] A.W. Fitzgibbon, Simultaneous linear estimation of multiple view geometry and lens distortion, in: *Proceedings of the IEEE Conference on Computer Vision and Pattern Recognition*, vol. 1, 2001, pp. 125–132.
- [10] R.I. Hartley, T. Saxena, The Cubic Rational Polynomial Camera Model, in: *Proceedings of the DARPA Image Understanding Workshop*, 1997, pp. 649–653.
- [11] D. Claus, A.W. Fitzgibbon, A rational function lens distortion model for general cameras, in: *Proceedings of IEEE Conference on Computer Vision and Pattern Recognition*, vol. 1, 2005, pp. 213–219.
- [12] D. Claus, A.W. Fitzgibbon, A plumbline constraint for the rational function lens distortion model, in: *Proceedings of the British Machine Vision Conference*, 2005.
- [13] T. Clarke, X. Wang, J. Fryer, The principal point and CCD cameras, *The Photogrammetric Record: An International Journal of Photogrammetry* 16 (92) (1998) 293–312.
- [14] R. Cipolla, T. Drummond, D. Robertson, Camera calibration from vanishing points in images of architectural scenes, in: *Proceedings of the British Machine Vision Conference*, vol. 2, 1999, pp. 382–391.
- [15] K. Daniilidis, J. Ernst, Active intrinsic calibration using vanishing points, *Pattern Recognition Letters* 17 (11) (1996) 1179–1189.
- [16] Y. Wu, Y. Li, Z. Hu, Detecting and handling unreliable points for camera parameter estimation, *International Journal of Computer Vision* 79 (2) (2008) 209–223.
- [17] G. Wang, J. Wua, Z. Jia, Single view based pose estimation from circle or parallel lines, *Pattern Recognition Letters* 29 (7) (2008) 977–985.
- [18] N.A.S. Murali, Perspective geometry based single image camera calibration, *Journal of Mathematical Imaging and Vision* 30 (3) (2008) 221–230.
- [19] J.Y. Zheng, S. Li, Employing a fish-eye for scene tunnel scanning, in: *Proceedings of the Asian Conference on Computer Vision*, 2006.
- [20] X. Ying, Z. Hu, H. Zha, Fisheye lenses calibration using straight-line spherical perspective projection constraint, in: *Proceedings of the Asian Conference on Computer Vision*, vol. 2, 2006, pp. 61–70.
- [21] C. Geyer, K. Daniilidis, Paracatadioptric camera calibration, *IEEE Transactions on Pattern Analysis and Machine Intelligence* 24 (5) (2002) 687–695.
- [22] X. Ying, Z. Hu, Can we consider central catadioptric cameras and fisheye cameras within a unified imaging model?, in: *Proceedings of the European Conference on Computer Vision*, vol. 1, 2004, pp. 442–455.
- [23] J.P. Barreto, H. Araujo, Geometric properties of central catadioptric line images and their application in calibration, *IEEE Transactions on Pattern Analysis and Machine Intelligence* 27 (8) (2005) 1327–1333.
- [24] J.P. Barreto, H. Araujo, Geometric properties of central catadioptric line images, in: *Proceedings of the European Conference on Computer Vision*, 2002, pp. 237–251.
- [25] A.W. Fitzgibbon, R.B. Fisher, A buyer's guide to conic fitting, in: *Proceedings of the British Machine Vision Conference*, 1995.
- [26] J.P. Barreto, H. Araujo, Fitting conics to paracatadioptric projections of lines, *Computer Vision and Image Understanding* 101 (3) (2006) 151–165.
- [27] R. Hartley, S.B. Kang, Parameter-free radial distortion correction with center of distortion estimation, *IEEE Transactions on Pattern Analysis and Machine Intelligence* 29 (8) (2007) 1309–1321.
- [28] S. Rajan, S. Wang, R. Inkol, Efficient approximations for the four-quadrant arctangent function, in: *IEEE Canadian Conference on Electrical and Computer Engineering*, 2006, pp. 1043–1046.
- [29] R. Strand, E. Hayman, Correcting radial distortion by circle fitting, in: *Proceedings of the British Machine Vision Conference*, 2005.
- [30] J.P. Barreto, K. Daniilidis, Fundamental matrix for cameras with radial distortion, in: *Proceedings of the IEEE International Conference on Computer Vision*, vol. 1, 2005, pp. 625–632.
- [31] J.-P. Tardif, P. Sturm, S. Roy, Self-calibration of a general radially symmetric distortion model, in: *Proceedings of the 9th European Conference on Computer Vision*, vol. 4, 2006, pp. 186–199.
- [32] C. Bräuer-Burchardt, K. Voss, Automatic lens distortion calibration using single views, in: *Mustererkennung, DAGM-Symposium*, September 2000, pp. 187–194.
- [33] F. Schaffalitzky, A. Zisserman, Planar grouping for automatic detection of vanishing lines and points, *Image and Vision Computing* 18 (9) (2000) 647–658.
- [34] R.I. Hartley, A. Zisserman, *Multiple View Geometry in Computer Vision*, second ed., Cambridge University Press, Cambridge, 2004.
- [35] D.W. Marquardt, An algorithm for least-squares estimation of nonlinear parameters, *SIAM* 11 (2) (1963) 431–441.
- [36] D. Ballard, C. Brown, *Computer Vision*, Prentice-Hall, Englewood Cliffs, NJ, 1982.
- [37] R. Waynant, M. Ediger, *Electro-Optics Handbook*, McGraw-Hill, New York, 2000.
- [38] K. Miyamoto, Fish eye lens, *Journal of the Optical Society of America* 54 (8) (1964) 1060–1061.